Journal of Aerosol Science 173 (2023) 106227

Contents lists available at ScienceDirect

Journal of Aerosol Science

journal homepage: www.elsevier.com/locate/jaerosci

Evolution of pore structure in nanoparticle deposits from unimodal to bimodal pore size distributions: Focus on structural features of dendritic structures

Jeonggeon Kim, Donggeun Lee *

School of Mechanical Engineering, Pusan National University, Busan, 46241, Republic of Korea

ARTICLE INFO

Handling Editor: Chris Hogan

Keywords:
Nanoparticle deposit
Monte Carlo simulation
Pore size distribution
Delaunay triangulation
Structural characteristics of dendrites and compact structure

ABSTRACT

Nanoparticle deposits can exhibit various structures, including compact and dendritic structures, depending on the deposition conditions. While previous studies have characterized deposit structures using factors such as porosity and spatial autocorrelation index, the pore size distribution (PSD), which is an essential structural property, has only been explored in compact structures. In this study, we investigate the PSDs of the entire nanoparticle deposits, ranging from compact to dendritic structures. Deposits are formed using an off-lattice Monte Carlo simulation, and deposition conditions are represented by two dimensionless numbers (Kn_D, χ_F). The diffusive Knudsen number (Kn_D) ranges from $10^{-1.5}$ to $10^{1.5}$, while the dimensionless translational energy of a particle (χ_F) ranges from 10^{-3} to $10^{1.5}$. We use the Delaunay triangulation algorithm for fast PSD calculation, and validate the calculation method using theoretical values of ideal structures and experimental literature data. Our results show that bimodal PSDs appear under thermally-dominated conditions with high values of Kn_D, while unimodal PSDs with a constant mode radius (~2.5 r_p) are observed under highly advective conditions with high values of χ_F. We present the geometric mean radii and mode radii of pores as color-filled contours to show their variation trends with Kn_D and χ_F. Additionally, we propose a simple model that predicts dendrite width by combining the overall porosity and mode radii of pores. Our model's predictions reasonably match the dendrite width data obtained using a density-based clustering algorithm.

1. Introduction

Aerosol nanoparticles can form different deposit structures depending on the deposition conditions, such as gas temperature and pressure, and particle size. The structural characteristics of nanoparticle deposits can affect their physical properties, such as electric conductivity (Castillo et al., 2014) and thermal conductivity (Lee & Hogan, 2021), and can enhance the system performance in applications such as boilers (Cai et al., 2018), sensors (Tricoli et al., 2008), and catalysts (Baturina & Wnek, 2005). Therefore, understanding the relationships between the structural characteristics of the deposits and the deposition conditions is essential to predict or improve system performance. Nuvoli et al. (2021) experimentally measured the overall porosity of nanoparticle deposits, which is the only wide-ranging experimental study to date. The scarcity of experimental studies highlights the difficulty in identifying the microstructure of nanoparticle deposits in terms of their porosity and pore size distribution. Thus, most studies have relied on

* Corresponding author.
E-mail address: donglee@pusan.ac.kr (D. Lee).

https://doi.org/10.1016/j.jaerosci.2023.106227
Received 1 May 2023; Received in revised form 12 June 2023; Accepted 13 June 2023
Available online 16 June 2023

numerical simulations (Castillo et al., 2014; Kim et al., 2022; Li et al., 2009; Lindquist et al., 2014; Madler et al., 2006; Nasiri et al., 2015; Lee & Hogan et al., 2021; Rodriguez-Perez et al., 2005; Tassopoulos et al., 1989).

Lindquist et al. (2014) investigated the variations in packing density of nanoparticle deposits under different deposition conditions using Langevin dynamics simulation. They represented deposition conditions with the diffusive Knudsen number (Kn_D) and dimensionless translational energy (χ_F), and presented a contour plot of packing density on the χ_F-Kn_D plane. This was the first result to relate the property of nanoparticle deposits to deposition conditions. However, the overall packing density alone does not represent microstructural characteristics of the deposits such as compact vs dendritic structures (Kim et al., 2022) or pore size distribution. Very recently, Kim et al. (2022) proposed a new method to visualize the distinctive difference between compact and dendritic structures. Unlike the conventional horizontal-average porosity, they presented local (vertical-average) porosity distribution (contour) with different colors to visualize the structural features of the deposits. They further calculated the spatial autocorrelation on the local porosity contour to classify the nanoparticle deposits into dendritic, intermediate, and compact structures. Notably, these studies enabled a priori prediction of the overall porosity and the apparent structure of the deposits from the deposition conditions (Kn_D, χ_F).

When it comes to the pore size distribution (PSD) of nanoparticle deposits, the PSD has become the last (unpredictable) key factor that can directly influence the thermophysical properties of the deposits. According to Zeng et al. (1994), the small pore size (10–100 nm) in mesoporous silica aerogel effectively limits the motion of gas molecules, reducing the apparent gas conductivity to a very low level. Thus, effective thermal conductivities of gas-particle binary systems may vary with pore size, even when the overall porosity is invariant. Shin et al. (2003) and Cherevko and Chung (2011) claim that the bimodal PSD consisting of micron and nanometer pores is beneficial for both the rapid transport of reactants and the increase of surface active sites in catalysts. Wang et al. (2021) examined droplet behavior in the cathode-side gas diffusion layer of a proton exchange membrane fuel cell and succeeded in reducing the pressure drop by 25.2–34.3% when applying a gradient pore size distribution for the gas diffusion layer. However, the problem is that it is not well known how PSD varies with deposition conditions. Furthermore, calculating the PSD of a nanoparticle deposit itself is not easy, particularly in the case of open-pore structures such as dendrites.

Prior to calculating the PSD of nanoparticle deposits, three structural features should be considered. Firstly, the overall porosity of nanoparticle deposits is typically high, ranging from 85 to 98%, compared to coarse-particle deposits which have a porosity of around 60% (German, 2014). As a result, calculating the PSD for deposit structures with such high porosity is very rare. Secondly, micro and meso pores in nanoparticle deposits are interconnected, which makes it difficult to define the pores in terms of their sizes, location, and boundaries. Therefore, it has become common to obtain the PSD using the concept of void particles that describe pores as virtual particles located inside the void space (Tassopoulos et al., 1989). Primera et al. (2003) calculated the PSD using the triangulation method in pore space, but this was only applicable to two-dimensional systems. Al-Raoush et al. (2003) compared two algorithms, the medial axis approach by pixelization and Delaunay triangulation, to identify pore networks in several regular packing of solid spheres (particles) and their random packing. As a result, both methods produced consistent pore structures for the regular packing, whereas the medial axis approach showed a discrepancy from Delaunay triangulation for the random packing, especially when the packing structure was pixelized to low resolution. Moreover, both methods tended to create multiple virtual spheres in a single void space (pore), requiring various merging methods to be developed. It is also questionable whether these methods could be applied for nanoparticle deposits because those methods were originally developed for consolidated structures such as sandstones, clays, and rocks with porosities below 60%. Bhattacharya and Gubbins (2006) developed a model to find the largest inscribed (virtual) sphere, centered at a random location in a void space, that just touches surrounding solid spheres with no overlap. However, all of these methods based on virtual particles are known to essentially underestimate the overall porosity of real irregular pore spaces (Xiong et al., 2016). Thirdly, nanoparticle deposits are speculated to have a distinctive PSD depending on their microstructures, between compact and dendritic structures. Unlike compact structures where pores are relatively uniform in shape and distributed with a single mode in size, dendritic structures may have a bimodal PSD arising from the coexistence of internal micropores in a dendrite and external mesopores between dendrites. To the best of our knowledge, there is no literature reporting the PSD characteristics of nanoparticle deposits varying from compact to dendritic structures.

Lee and Hogan (2021) conducted numerical simulations to investigate the porosity and PSD of nanoparticle deposits produced under more realistic circumstances such as polydispersity, coalescence, and aggregation of nanoparticles. It is noteworthy that their simulated nanoparticle deposits always exhibited unimodal PSDs unless the particles agglomerated into large aggregates prior to deposition. Applying their 12 combinations of Kn_D and χ_F to Kim et al. (2022)'s model, the deposition conditions they considered can only produce compact or intermediate deposit structures. Hence, the purpose of this study is to investigate the variations in the pore structure of nanoparticle deposits encompassing the compact-to-dendritic structures through numerical simulations and to quantitatively present the characteristics of the PSDs. Additionally, we calculate new structural properties of nanoparticle deposits, such as dendrite width, combining the PSD with overall porosity.

2. Off-lattice Monte Carlo simulation to create nanoparticle deposits

2.1. Deposition condition

Three-dimensional off-lattice Monte Carlo (MC) simulation was performed to produce the deposit structures under various deposition conditions. MC simulation imitates the motion of aerosol nanoparticles by dividing it into two types of motion: thermal and advective motion. Thermal motion is a random walk of nanoparticle caused by many collisions with gas molecules, leaving behind a meandering trajectory, and is generally measured by the persistent distance of particle in its thermal motion. Advective motion

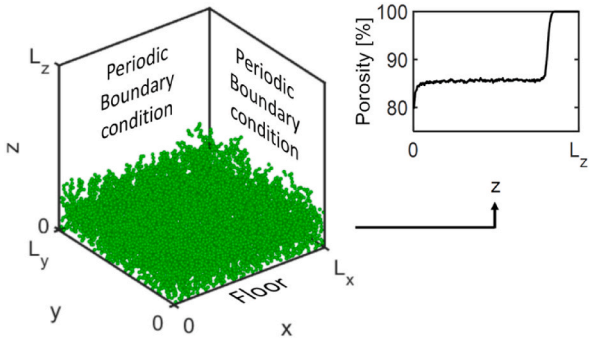

Fig. 1. Diagram of the computation domain for off-lattice Monte Carlo simulations, with the coordinate system. The inset displays the porosity profile along the height (z) of the particle deposit. The bottom layer, formed on the floor substrate, exhibits a rapid increase in porosity with height, whereas the middle layer is defined as the region where the porosity remains almost constant with height. The top layer represents the rough surface of the deposit, where the porosity increases again due to the presence of open surface pores.

represents a translational motion driven by external forces such as thermophoretic, gravitational, or electrostatic forces. The two motions were characterized by two dimensionless numbers in Eqs. (1a) and (1b) (Hunt et al., 2014; Kim et al., 2022; Lindquist et al., 2014).

$$Kn_D = \frac{\lambda_p}{r_p} = \frac{\sqrt{m_p k_B T}}{f r_p} \tag{1a}$$

$$\chi_F = \frac{m_p v_{ad}^2}{k_B T} \tag{1b}$$

where Kn_D, the diffusive Knudsen number of particles, describes the ratio of the particles' persistent distance (λ_p) to their radius (r_p). m_p represents the particle mass. The friction coefficient (f) of the particles is determined using Stokes' law with the Cunningham slip correction factor (C_c) as $f = 6\pi\mu r_p / C_c$, where $C_c = 1 + Kn(A_1 + A_2\, exp[-2A_3/Kn])$ (Mädler & Friedlander, 2007). The values of $A_1 = 1.257$, $A_2 = 0.40$, $A_3 = 0.55$, and Knudsen number (Kn) of gas are used. T is temperature of surrounding gas. χ_F is defined as the ratio of translational energy of particles to thermal energy to represent the relative significance of advective motion of particles. When $Kn_D \geq 10^0$ and $\chi_F \leq 10^{-1}$, the thermal motion dominates the advective motion, which is referred to as the thermally-dominated condition in this study. Conversely, the highly advective condition represents the case where the particle behavior upon deposition is determined mainly by advective motion (e.g., $\chi_F \geq 10^1$).

2.2. Procedure of MC simulation

To simulate the movement of a particle, we considered the displacement ($\Delta\vec{s} = \vec{s}(t+\Delta t) - \vec{s}(t)$) from a position $\vec{s}(t)$ at time t to the next position $\vec{s}(t+\Delta t)$ after a time interval of Δt. The displacement was expressed as the vector sum of diffusive displacement ($\vec{l}_{diff}$) and advective displacement ($\vec{l}_{ad}$) in Eq. (2) for MC simulation (Kulkarni & Biswas, 2004).

$$\vec{s}(t+\Delta t) = \vec{s}(t) + \vec{l}_{diff} + \vec{l}_{ad} \tag{2}$$

In Eq. (2), the vector $\vec{l}_{ad}$ was simply calculated as the product of the advective velocity ($\vec{v}_{ad}$) and the time interval (Δt) in response to the external force acting on the particle toward the deposition surface, specifically in the negative z direction in the coordinate system of Fig. 1. The random displacement vector $\vec{l}_{diff}$ by diffusion was obtained by generating random numbers for each vector component in accordance with the Gaussian distribution. Each vector component corresponding to a coordinate axis has an average of zero and a standard deviation of $\sqrt{2D\Delta t}$ (Kim et al., 2022; Kulkarni & Biswas, 2004). Here, the particle diffusivity (D) was calculated as $k_B T / f$ (Hinds, 1999, p. 152). To take into account the particle's inertia and consider its realistic movement, we set Δt to be three times the particle relaxation time ($\Delta t = 3\tau_p = 3m_p/f$) as recommended by Moran et al. (2020) (will be addressed in greater detail at the end of this section).

Fig. 1 illustrates the calculation domain used for the MC simulation. The deposition surface (floor in Fig. 1) was built on the horizontal xy-plane, and the bottom surface was as large as $1000r_p \times 1000r_p$. The periodic boundary condition was applied along the sidewalls of the three-dimensional calculation domain. The inset in Fig. 1 shows the variation of porosity along the deposit height z, typically displaying an S-shaped curve. The porosity in the inset represents the average porosity of a horizontal slice located at z. In the middle layer of the deposit, the porosity is constant with height z. This constant porosity is referred to as the overall porosity $\overline{\Theta}_{pore}$, which represents the characteristics of the whole deposit layer (Lindquist et al., 2014; Rodriguez-Perez et al., 2007). Because the middle layer occupies most of the volume of the deposit as deposition progresses, all discussions in this study about the deposit

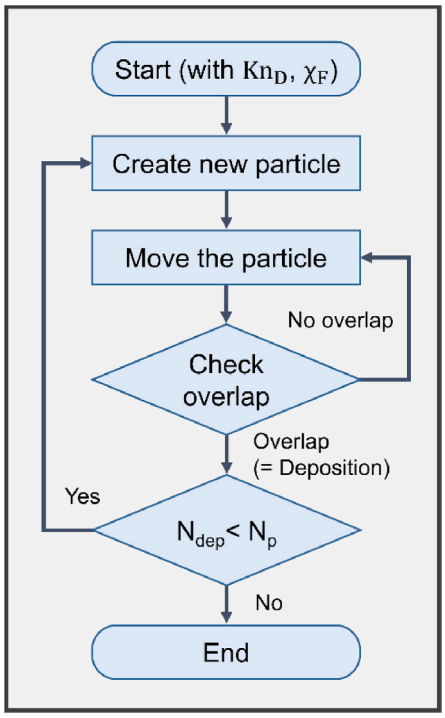

Fig. 2. Flow chart of the off-lattice Monte Carlo simulations.

structures will focus on the middle layer unless otherwise stated.

MC simulation was conducted following the flowchart in Fig. 2, which refers to the simulation procedure used in our previous work (Kim et al., 2022). First, a particle was randomly created on a horizontal xy-plane located $3(\sqrt{2D\Delta t}+l_{ad})$ above the top of the deposit. Second, the particle ballistically moved to the next position calculated using Eq. (2) for Δt. Third, if any pre-existing deposited particle was encountered along its rectilinear path, the moving particle was set to slightly retreat and adhere to it at the first contact point, in order to maintain a point contact. Last, the process was repeated until the number of deposited particles (N_{dep}) reaches the target number (N_p). As the deposition condition approaches a thermally-dominated condition, the deposit layer becomes increasingly roughened with the appearance of individual dendrites, requiring more particles to be deposited to exhibit a stable porosity. In this study, the value of N_p for dendritic structures was around 2.4×10^7, which is larger than 6.5×10^6 for compact structures. It should also be noted that the deposition condition considered in this study is broad, encompassing a range of $10^{-1.5} - 10^{1.5}$ for Kn_D and $10^{-3} - 10^3$ for χ_F (49 cases in total). The range of Kn_D covers most of the nanoparticles (in a range of 5 nm–1 μm) used in the environment and energy fields. The MC simulation was repeated three times to obtain a stable value for each case.

Referring again to Kim et al. (2022), we calculated the local porosity, $\Theta_{pore}(x^*,y^*)$, to visualize the structural features of nanoparticle deposits from compact to dendritic structures on a dimensionless surface, where the asterisk (*) denotes non-dimensionalized variables with r_p. Specifically, we obtained the local porosity distribution contours by slicing the middle layer of deposits into a large number of vertical rectangular prisms and calculating the vertical average porosity for each prism at its local position (x^*,y^*). Since each prism had a square top and bottom with a side length equal to the particle diameter $(\Delta x^* = \Delta y^* = 2)$, the local porosity distribution data were naturally displayed as gray contours with a resolution of 500×500. Moreover, we further calculated the spatial autocorrelation index (I) for the resulting local porosity distribution contours to identify the structures among compact, intermediate, and dendritic structures. For reference, in the case of randomly dispersed local porosity, the index I becomes zero, which represents the spatial randomness or independence of the dispersed spots. On the contrary, the closer the index I is to $+1$, the more similar (highly correlated) regions are found.

Now, let us address the significance of using the specific timestep $\Delta t = 3\tau_p$ in our MC simulations for constructing nanoparticle deposits. In fact, the algorithm for updating the diffusive displacements (l_{diff}) in Eq. (2) follows the diffusive limit where $Kn_D \to 0$ as in the continuum regime (Lindquist et al., 2014). In contrast, modern Langevin dynamics simulations (Gopalakrishnan & Hogan, 2011; Lindquist et al., 2014; Madler et al., 2006) are known to accurately simulate the Brownian motion of nanoparticles in the transition regime without the restriction of $Kn_D \to 0$. In most Langevin dynamics simulations, a sufficiently small timestep has typically been used to accurately predict the stochastic random displacements of particles, such as $\Delta t \leq 0.005 Kn_D^{-2}$ in dimensionless form (Gopalakrishnan & Hogan, 2011). However, this, in turn, makes Langevin dynamics simulations computationally expensive especially under thermally-dominated conditions. Meanwhile, Moran et al. (2020) discretized a meandering trajectory of a particle obtained through Langevin dynamics simulation into multiple broken line segments to mimic MC simulations. By examining the probability distribution

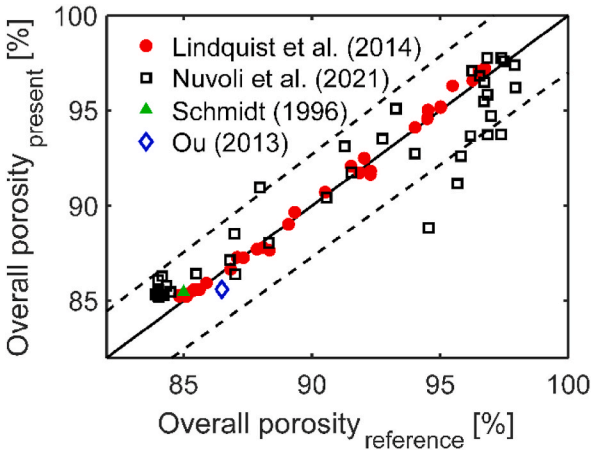

Fig. 3. Direct comparison of the overall porosity data obtained by the present MC simulations with those from literature. The solid symbols represent the results from previous simulation studies (Lindquist et al., 2014; Schmidt, 1996), while the hollow symbols indicate experimental results reported in the literature (Nuvoli et al., 2021; Ou, 2013). The solid line implies a perfect match between the present MC simulations with the literature data, and the dashed lines indicate ± 3% relative error band.

for the angle between two successive line segments, they discovered that using a small discretization timestep (corresponding to our Δt) results in a volcano-shaped probability distribution that peaks at an angle of zero. This suggests that particle displacements in reality are not randomly oriented during the short timestep. This can be understood from the solution of Langevin equation, where the velocity and displacement of particles are not independent of each other but rather statistically correlated (Ermak & Buckholtz, 1980). Interestingly, Moran et al. (2020) reported that the particle displacements become random when $\Delta t \to \infty$, which is consistent with our approach in Eq. (2). Here, it is worth noting that Kulkarni and Biswas (2004) used a sufficiently long timestep for their MC simulations as $\Delta t \gg \tau_p$. On the other hand, the timestep needs to be shortened to properly track the particle trajectory calculated by Langevin dynamics simulation. In fact, Moran et al. (2020) discovered that $\Delta t = 3\tau_p$ is the minimum acceptable timestep which allows MC simulations to accurately capture nanoparticles' random walks in comparison with Langevin dynamics simulation, spanning from the free molecular to continuum regimes. This is why we utilized the redefined persistent distance (l_{diff}) of nanoparticles by diffusion, following a Gaussian distribution with a standard deviation of $\sqrt{2D\Delta t}$ in one direction, which corresponds to $\sqrt{18D\tau_p}$ in three dimensions, as recommended by Moran et al. (2020). Thus, the random displacement (l_{diff}) for 3 τ_p in Eq. (2) becomes $\sqrt{18m_p k_B T}/f$ in three dimensions, which is larger than the conventional persistent distance λ_p in Eq. (1a).

When it comes to the initial positioning of a new particle in the first step of MC simulations, one may need to minimize the positioning height while deposit structures are unaffected. This is because nanoparticles' random walks can significantly increase the simulation time, especially under thermally-dominated conditions. As demonstrated in our previous work (Kim et al., 2022), we defined the z-axis position to release a new particle as $N(\sqrt{2D\Delta t} + l_{ad})$ from the top of the deposit. In a preliminary test, we increased N from 1 to 9 and observed that there was no significant dependence on N for both the overall porosity and spatial autocorrelation index when $N \geq 3$. It is also noteworthy that the selected positioning height $3(\sqrt{2D\Delta t} + l_{ad})$ ensures a similar number of minimum steps required to reach either the bottom surface or the top of pre-deposited layer, regardless of deposition conditions.

2.3. Validation

The MC simulation was validated by comparing the predicted overall porosity with existing literature data (Lindquist et al., 2014; Nuvoli et al., 2021; Ou, 2013; Schmidt, 1996). Lindquist et al. (2014) calculated the overall porosity using Langevin dynamics simulation with a large calculation domain ($1000\, r_p \times 1000 r_p$) under various deposition conditions ($10^{-3} \leq Kn_D \leq 10^{1}$; $10^{-4} \leq \chi_F \leq 10^{3}$). Nuvoli et al. (2021) experimentally measured the overall porosity of deposits formed by depositing 62-, 87-, and 108-nm KCl particles at 1 atm or 62-nm CsCl particles at 0.5 and 1 atm. In Fig. 3, the solid symbols (red and green) represent the existing simulation results, while the hollow symbols (black and blue) represent the experimental data taken from literatures. The solid line in the figure indicates the perfect match between the present simulation and the existing literature data. As a result, our simulation results are in good agreement with the existing simulation data with a maximum error of 0.8% and an average error of 0.3%. However, our simulation makes less accurate predictions of the overall porosity for the experiments, such as with a maximum error of 6.0% and an average error of 1.6%. Excluding a few data points from Nuvoli et al. most of experimental data lies within a ±3% error range, denoted by two dashed lines in the figure. Consequently, this validation result likely reaffirms the validity of our approach in relation to Eq. (2) under all conditions of Kn_D and χ_F.

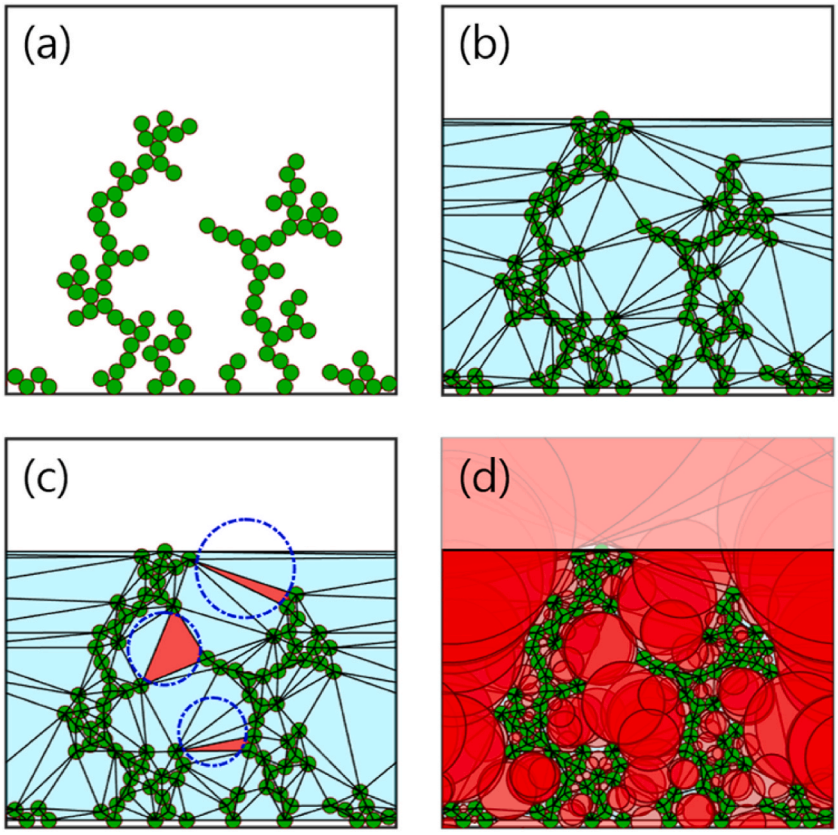

Fig. 4. Graphical illustration of the process of Delaunay triangulation and subsequent calculation of volume and size of individual pores in a nanoparticle deposit: (a) An exemplified microstructure of the nanoparticle deposit projected onto a vertical (x–z) plane, (b) Division of the pore space into numerous tetrahedrons using the Delaunay triangulation method, (c) Fast identification of the inscribed sphere for each tetrahedron to estimate its size, and (d) Visualization of the inscribed spheres in red color. (For interpretation of the references to color in this figure legend, the reader is referred to the Web version of this article.)

3. Pore size distribution (PSD)

3.1. Calculation method

To the best of our knowledge, Dreyer et al. (2014) and Lee and Hogan (2021) are the only existing studies that have dealt with a numerical methodology for calculating PSDs of *nanoparticle* deposits. Dreyer et al. (2014) used an image-based method suggested by Yang et al. (2009), which involves cutting a porous deposit layer into thin horizontal slices and digitizes each two-dimensional slice into pixels. Then, they calculated the maximum radius of a virtual sphere that fits the void space at the center of each pixel without overlapping with surrounding solid particles. Although PSD calculations in three dimensions are essentially possible by combining the result with those of neighboring slices, the accuracy of this method is limited by image resolution. Moreover, the computational load becomes large when applied to a large calculation domain such as $1000\, r_p \times 1000 r_p$ in our study. Lee and Hogan (2021) used the open source code of Bhattacharya and Gubbins (2006) for PSD calculation. This method repeats finding the largest inscribed sphere at random points inside a void space of nanoparticle deposits, thereby reducing the calculation load by sampling the positions to probe instead of probing every pixel. However, this sampling process is prone to a lack of information on pore positions and was validated only for a small calculation domain of $50\, r_p \times 50\, r_p$ under limited deposition conditions that preferentially generate the *compact* deposit layers (Kim et al., 2022; Lee & Hogan, 2021). In contrast, our study deals with deposition of millions of nanoparticles in a much larger calculation domain and covers a variety of deposit layers ranging from dendritic to compact structures. Thus, it may require another method that can more efficiently calculate PSDs of these various porous structures.

In this study, the Delaunay triangulation was employed using the incremental algorithm to analyze the pore structures of nanoparticle deposits. For a given set P of n points in a space, Delaunay triangulation divides the space into multiple tetrahedrons (or triangles in two dimensions) by connecting the points in a way that satisfies the Delaunay condition: the intersection of two tetrahedrons is either empty or a vertex or an edge or a face; and none of the tetrahedrons contains any of the given points in its interior (Sloan, 1993). The PSD calculation procedure used in this study is as follow. Once all particles are deposited, they are firstly treated as points given at their center coordinates in the three-dimensional deposit layer (see Fig. 4(a)). Then, Delaunay triangulation is

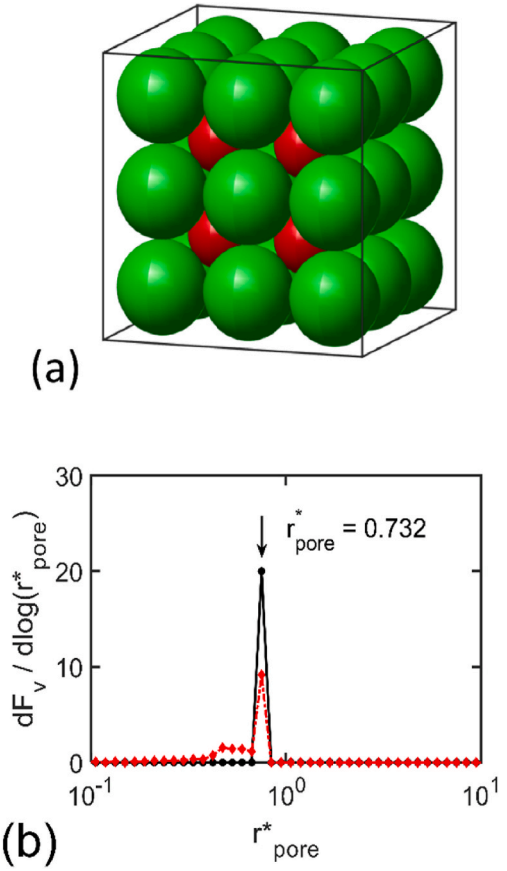

Fig. 5. Calculation of pore size distribution for a simple cubic structure of closely-packed size-monodisperse particles: (a) A graphical illustration of the pristine (green) particles and the resulting small (red) pores between particles, and (b) Comparison of the PSD obtained by the present method (solid line) with that from the literature (dotted line) (Bhattacharya & Gubbins, 2006). (For interpretation of the references to color in this figure legend, the reader is referred to the Web version of this article.)

implemented in accordance with the procedure described in Appendix A, resulting in numerous tetrahedrons as exemplified in Fig. 4 (b). Since four vertices of each tetrahedron are specified, it is straightforward to construct its circumscribed sphere as well as the sphere inscribed by the four same-sized particles located at the vertices, as illustrated by dotted circles in Fig. 4(c). The radius of the inscribed sphere is readily obtained by subtracting the particle radius from the radius of the same-centered circumsphere. Fig. 4(d) displays the inscribed spheres of the entire tetrahedrons with red color, such that the void space seems to be completely filled with the red spheres. It should be noted that any inscribed sphere is used only for sizing the corresponding pore, whereas the pore volume is obtained from the volume of the tetrahedron upon excluding the part occupied by the particles, according to Appendix B (as highlighted with red-filled triangles in Fig. 4(c)). As such, there is no need of finding the largest inscribed spheres through sampling or conditional merging algorithm of those spheres used in the existing literatures (Al-Raoush et al., 2003; Tassopoulos et al., 1989), which enables fast calculation of PSDs.

Based on the dataset of radii (r_{pore}) and volumes (V_{pore}) of all (tetrahedral) pores obtained through the foregoing procedure, the pore size distribution function (f_v) can be expressed as

$$f_v = \frac{dF_v}{d\log\left(r^*_{pore}\right)} \cong \frac{\Delta\left(\sum V_{pore}/V_{pore,total}\right)}{\Delta\log\left(r^*_{pore}\right)} = \frac{\Delta\left(\sum \Theta_{pore}/\overline{\Theta}_{pore}\right)}{\Delta\log\left(r^*_{pore}\right)} \tag{3}$$

where r^*_{pore} is a dimensionless pore radius defined by (r_{pore}/r_p), $\sum V_{pore}(\le r_{pore})$ is the sum of volumes of pores whose radii are smaller than or equal to r_{pore}, and F_v is the cumulative volume fraction of pores with respect to the total volume of pores ($V_{pore,total}$). Therefore, $dF_v = f_v d\log(r^*_{pore})$ represents the volume fraction of pores ranging from $\log(r^*_{pore})$ to $\log(r^*_{pore}) + d\log(r^*_{pore})$. Dividing $\sum V_{pore}$ and $V_{pore,total}$ by the apparent volume of the deposit (V_{app}) including the pores, respectively, yields the cumulative porosity ($\sum \Theta_{pore}$) and overall porosity ($\overline{\Theta}_{pore}$) as shown in Eq. (3). Thus, the area under the curve of f_v in the entire range of r^*_{pore} is always unity. The bin size $\Delta\log(r^*_{pore})$ was set to be constant at 0.05.

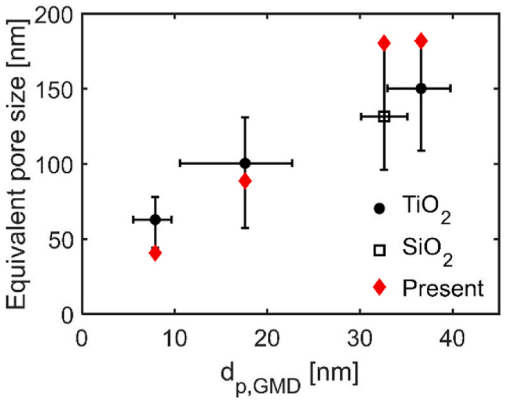

Fig. 6. Comparison of the average pore diameters calculated for the top layer using the present method with the approximate equivalent pore diameters obtained from top-view SEM images (Kubo et al., 2013), where $d_{p,GMD}$ represents the geometric mean diameter of particles.

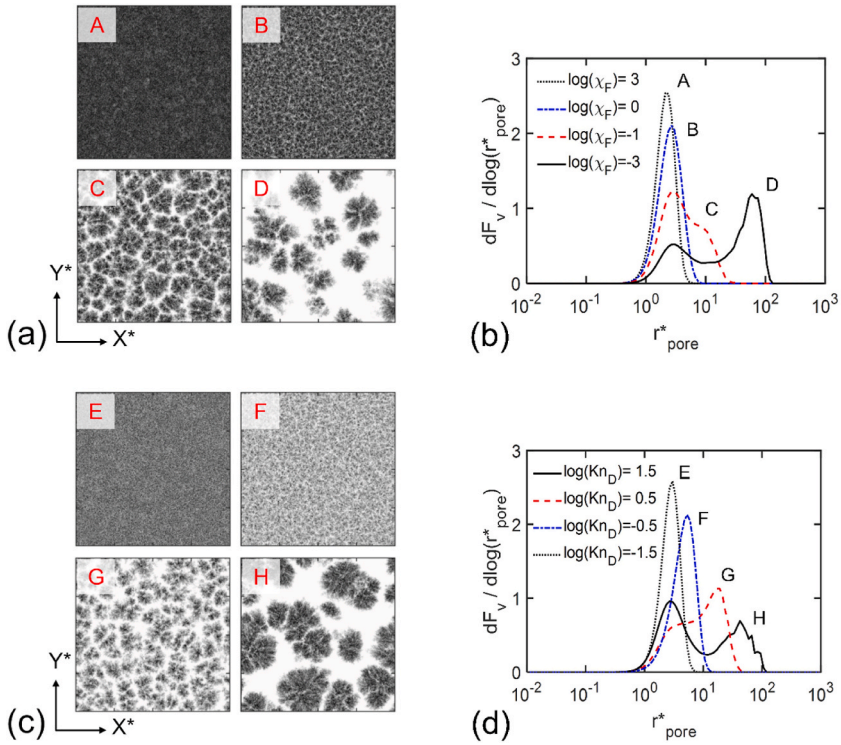

Fig. 7. Variations in the local porosity distribution contours and the corresponding pore size distributions of nanoparticle deposits under different deposition conditions: (a) Local porosity distribution contour plots for the deposits produced in Cases A-D, (b) Pore size distribution profiles calculated for the structures shown in (a), (c) Local porosity distribution contours in Cases E-H, and (d) The corresponding PSD profiles for the structures shown in (c).

3.2. Validation

The method described in Section 3.1 was applied to obtain the PSD profile for a simple cubic structure of size-monodisperse particles. Fig. 5(a) illustrates the ideal packing of green particles and the resulting spherical pores in red color precisely located at the centers of unit cubes. The red pores are the largest spherical ones, best fitted in the void space with a theoretical radius of $0.732r_p$ and a theoretical volume fraction of pores (i.e. porosity) of 47.64% (Kruyer, 1958). For the cubic structure comprising approximately 100,000 particles, we calculated the PSDs using the present method described in Section 3.1 and Bhattacharya & Gubbins' (BG) method (2006) for comparison. As depicted in Fig. 5(b) with the solid line, the present method predicted a unimodal PSD with a very sharp single spike, indicating that all the spherical pore sizes are not distributed but monodisperse in size at $r^*_{pore} = 0.732$ within the bin

Table 1
Summary of deposition conditions for constructing nanoparticle deposits and their structural properties. If PSD is unimodal, the only mode radius is recorded on the 'Left' column.

Cond.	Kn_D	χ_F	$\overline{\Theta}_{pore}$	I	$r^*_{pore,mode}$	
					Left (Primary)	Right (Secondary)
A	10^1	10^3	85%	0.22	2.2	–
B	10^1	10^0	87%	0.53	2.6	–
C	10^1	10^{-1}	91%	0.82	2.7	11
D	10^1	10^{-3}	96%	0.92	2.7	85
E	$10^{-1.5}$	10^{-2}	89%	0.33	2.9	–
F	$10^{-0.5}$	10^{-2}	94%	0.61	5.1	–
G	$10^{0.5}$	10^{-2}	95%	0.85	3.3	19
H	$10^{1.5}$	10^{-2}	93%	0.90	2.7	52

size, which is identical to the theoretical radius. Additionally, the overall porosity ($\overline{\Theta}_{pore} \equiv V_{pore,total}/V_{app}$) was 47.64%, consistent with the theoretical porosity. In contrast, when using the BG method, the PSD exhibits a bimodal distribution with a left tail (as shown by the dotted line in Fig. 5(b)). This tail arises from filling a narrow void space (between two adjacent particles and their inscribed (major) pore) with smaller pores. Thus, the BG method appears to slightly underestimate the mean pore size compared to the triangulation-based method currently in use, which is consistent with previous findings by researchers (Morales-Flórez et al., 2008; Storchi et al., 2015). In particular, the calculation time of the BG method was 10 min using a bin size of 0.25 r_p in linear scale. However, this sharply increased to 115 min when the bin size was decreased to 0.01 r_p to improve accuracy, which is much longer than 70 s required by the present method. It is noted that this comparison was conducted using Intel i7-5820 K CPU and 16 GB RAM.

To further validate our method, we compared the average pore diameters we obtained with the experimental data from a previous study conducted by Kubo et al. (2013). In their study, they presented SEM images of TiO_2 or SiO_2 spherical-nanoparticle deposits prepared under different deposition velocities using electrostatic deposition. They approximated the void area on the top view images by circles that fit the void area, and calculated the equivalent pore diameter per image by counting the circles in terms of their diameters. To simulate their experimental conditions as closely as possible, we characterized their deposition conditions in terms of χ_F and Kn_D, based on the gas/particle properties and the geometric mean diameter of the particles they provided. We then performed MC simulations for the conditions of χ_F and Kn_D. As Kubo et al. obtained the equivalent pore diameters from the top-view images, we only considered the upper layer located on top of the middle layer for PSD calculations. Our results, shown as red diamonds in Fig. 6, demonstrate that the average pore diameters we obtained are in reasonable agreement with the experimental data (represented by black symbols) within the margin of error.

4. Results and discussion

Fig. 7 shows the contours of the local porosity distribution and the PSD profiles of nanoparticle deposits formed under various deposition conditions. The deposition conditions are summarized in Table 1, which covers a wide range of overall porosities $\overline{\Theta}_{pore}$ (85%–97%) and structures (dendritic-to-compact) of nanoparticle deposits.

In Fig. 7(a), the local porosity distribution data are presented as contours plotted in gray, as χ_F decreases from 10^3 to 10^{-3}, while Kn_D remains fixed at 10. The white color indicates empty space with 100% local porosity, while the color becomes darker in proportion to the solid fraction (i.e., 1 - local porosity). Under the highly advective condition of $\chi_F = 10^3$ (Case A in Table 1), the top-left figure in Fig. 7(a) shows randomly distributed dark gray dots, indicating the formation of a compact deposit structure. While χ_F decreases to 1 (Case B), there is no distinct difference in the contour plot. However, further decrease in χ_F (Cases C and D) results in a clear transition from a compact to a dendritic structure as highlighted in Case B-to-D of Fig. 7(a). We also calculated the spatial autocorrelation (I) for the local porosity contours in Fig. 7(a) and listed them together with the $\overline{\Theta}_{pore}$ in Table 1. In the diagram of compact structures, local porosity contours appear as randomly distributed tiny dots, representing a random structure with little autocorrelation, so the I index approaches to zero. In contrast, dendritic structures exhibit self-similar dendrites, which increase the I index to unity (Zhang & Lin, 2007). In fact, Table 1 shows that the I index continually increases from 0.22 to 0.92 along with the aforementioned structural change.

Fig. 7(b) shows the PSD profiles corresponding to the four cases presented in Fig. 7(a). Under a highly advective condition where $\chi_F = 10^3$, the PSD is unimodal with a mode radius of $2.2r_p$ ($= 10^{0.35}r_p$). As χ_F decreases to unity (Case B), the PSD remains unimodal but broadens slightly, with a slight increase in the mode radius to $2.7r_p$ ($= 10^{0.44}r_p$). Further decreasing χ_F (resulting in diffusive deposition) leads to a clear transition of PSD from unimodal to bimodal, with the appearance of large pores in Cases C and D. Notably, when $\chi_F = 10^{-1}$, the PSD widens significantly due to the separation of a half-height shoulder from the original single peak. From Case C to D, the hidden secondary peak at the shoulder becomes more prominent with a larger shift. Of particular interest is to note that the primary (left) mode radius is relatively invariant at around 2.5 r_p in the four cases, while the secondary (right) peak continues to grow to larger sizes (8.3 r_p to 85 r_p) from Case C to D. In Case C, where the secondary peak appears, it is interesting to recall that the deposit structure began the structural transition by creating discernible cracks (see Case C in Fig. 7(a)). Likewise, Case D exhibits that the cracks have widened to form individual dendrites in Fig. 7(a) and, coincidentally, shows the growth of large pores in Fig. 7(b). This suggests that the secondary peak in the PSD might be associated with the empty space between dendrites, while the primary peak likely

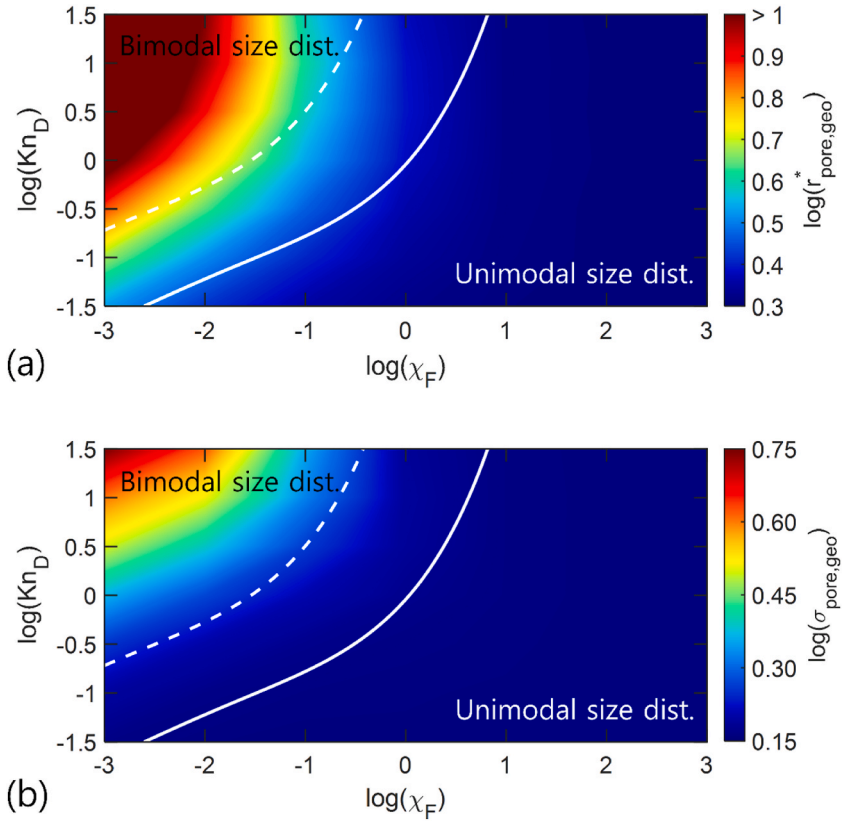

Fig. 8. Color-filled contour maps of (a) the geometric mean radius and (b) the standard deviation of pores in nanoparticle deposits plotted against Kn_D and χ_F. The solid line represents the boundary of the structural transition from the compact to intermediate structure, while the dashed line indicates the intermediate-to-dendritic structural transition boundary. (For interpretation of the references to color in this figure legend, the reader is referred to the Web version of this article.)

denotes the pore structure inside a single dendrite on average. To confirm this speculation, we created a similar dendritic structure and calculated the PSD separately for a single dendrite (marked as A in Fig. S1) and an empty space (marked as B). The result shows that the dendrite itself is microporous with a mode radius of ~2.7 r_p as shown in graph A in Fig. S1. In contrast, the empty space is mesoporous with a pore radius of ~50 r_p as shown in graph B. Therefore, it is evident that the bimodality observed in PSDs (such as Case D in Fig. 7 (b)) is a consequence of the formation of isolated dendrites.

In addition to Cases A-D, where χ_F varied, we conducted further investigations into the impact of Kn_D on the microstructure of nanoparticle deposits. Fig. 7(c) and (d) illustrate changes in local porosity contours and their PSD profiles as Kn_D increases from $10^{-1.5}$ to $10^{1.5}$ with $\chi_F = 10^{-2}$. In Case E, with $Kn_D = 10^{-1.5}$ (under the most advective condition), the nanoparticle deposit displays an overall porosity ($\overline{\Theta}_{pore}$) of 89%, a low autocorrelation (I) of 0.33, and a mode radius of 2.9 r_p (=$10^{0.47}$ r_p) in its PSD, indicating a compact structure with a unimodal PSD. When Kn_D is increased to $10^{-0.5}$ (Case F), the deposit layer still appears to exhibit a compact structure with a unimodal PSD, but shows a more noticeable peak shift (from 2.7 r_p to 5.1 r_p) in Fig. 7(d) compared to Cases A and B in Fig. 7(b). This suggests that the deposit layer created in Case F is more porous than in Case B, which is supported by the brighter image of Case F in Fig. 7(c) than that of Case B and the $\overline{\Theta}_{pore}$ in Table 1 ($\overline{\Theta}_{pore}$ = 94% in Case F vs 87% in Case B). As Kn_D increases further to Cases G and H, the nanoparticle deposit transforms into dendritic structures, as indicated by Fig. 7(c), which leads to a steady increase in I (0.85 and 0.90) without any discernible change in $\overline{\Theta}_{pore}$ (95% and 93%, respectively). Consistently, Fig. 7(d) reconfirms that the PSDs are correspondingly bimodal in Cases G and H, while the left-mode radius of pores returns to the mode radius of pores in the compact structure (Case E). It is noted that the PSD profile in Case F is asymmetric, slightly left-skewed in log scale, meaning that there might be a small hidden peak at the mode radius of Case E. Thus, the Case-F image of Fig. 7(c) seems to show the very beginning of structural transition by creating many but very small dendrites. However, the PSD profile was not further decomposed into two peaks but rather treated as a single unimodal peak to prevent any unexpected uncertainty issues.

Based on the PSD profiles ($f_v = dF_v/d\log(r^*_{pore})$ vs $\log(r^*_{pore})$), one can calculate the variation in the average pore radius by defining the geometric mean radius of pores $r^*_{pore,geo}$ as $\log(r^*_{pore,geo}) = \int_{-\infty}^{\infty} \log(r^*_{pore}) f_v d\log(r^*_{pore})$. We repeated the MC simulation for all combinations of (Kn_D, χ_F) conditions (49 cases in total and three times for each case) and plotted the resulting $r^*_{pore,geo}$ and the corresponding geometric standard deviation $\sigma_{pore,geo}$ as a color-filled contour with respect to Kn_D and χ_F in Fig. 8(a)–(b), respectively. In both Fig. 8(a)–

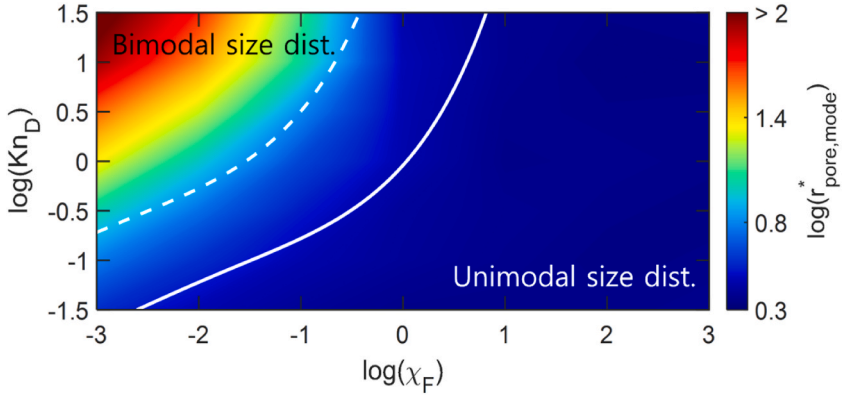

Fig. 9. Color-filled contour map of the mode radius of pores in nanoparticle deposits plotted against Kn_D and χ_F. In cases of bimodal pore size distributions, the right (secondary) mode radius was taken. (For interpretation of the references to color in this figure legend, the reader is referred to the Web version of this article.)

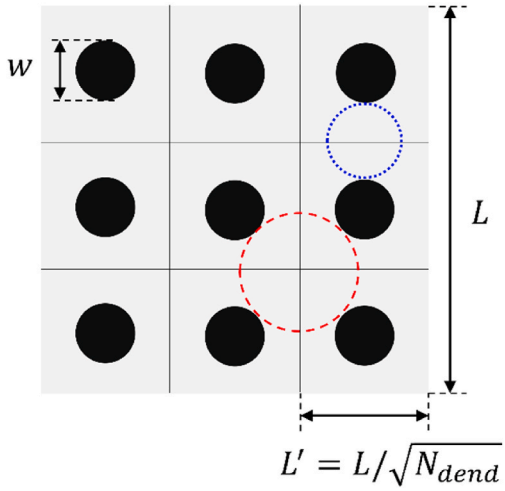

Fig. 10. Schematic diagram of a simple model used to predict the average width of dendrites (w). The black circles represent cross-sections of dendrites approximated as identical cylinders that are uniformly distributed. The dashed and dotted hollow circles represent two limiting distances between dendrites in this ideal system, suggesting that the average distance between two adjacent dendrites in real systems might be bounded by these two values.

(b), the green-to-red zone, which represents large mean radii of pores with wide size distributions, appears in the upper-left region, i.e., thermally-dominated conditions with high Kn_D and low χ_F. Referring to our previous work (Kim et al., 2022), the upper-left region, in particular, bounded by the dashed line, indicates the creation of dendrites, whereas the solid line divides the intermediate structure and compact structure. Overall, the sudden increase in the geometric mean radius of pores as well as their geometric standard deviations (highlighted by green to red colors) is closely related to the appearance of dendrites, although the green zone does not perfectly match the transition boundary indicated by the dashed line. Specifically, the compact structure, shown in deep blue, indicates a relatively invariant $r^*_{pore,geo}$ within the range of 2.0–2.5, along with a negligible variation in $\sigma_{pore,geo}$ ranging from 1.44 to 1.46. This behavior aligns with that observed in the unimodal PSDs shown in Fig. 7(b) and (d). As the deposition condition moves into the region of intermediate structures (between the solid and dashed lines), there is an increase in $r^*_{pore,geo}$ to 2.4–4.7 ($= 10^{0.39}$ - $10^{0.68}$), accompanied by a slight increase in $\sigma_{pore,geo}$ to 1.47–1.62 ($= 10^{0.17}$ - $10^{0.21}$). Moving to the thermally-dominated condition, $r^*_{pore,geo}$ significantly increases from 3.8 to 7.2 ($= 10^{0.58}$ - $10^{0.86}$) near the transition boundary to a maximum of 18 ($= 10^{1.26}$). Simultaneously, $\sigma_{pore,geo}$ also exhibits a pronounced increase, ranging from 1.81 to 2.26 ($= 10^{0.26}$ - $10^{0.35}$) near the transition boundary to a maximum of 5.62 ($= 10^{0.75}$).

In addition to the average pore radius ($r^*_{pore,geo}$), the two mode radii ($r^*_{pore,mode}$) are extracted from all bimodal PSDs. However, it should be noted that the bimodal PSD profiles are not decomposed into two sub peaks to further calculate their corresponding geometric standard deviations ($\sigma_{pore,geo}$). Instead, we solely focus on the two mode radii to avoid any potential uncertainty issues that may arise from peak deconvolution. Fig. 9 presents a color-filled contour plot that shows either the single mode radius for the unimodal

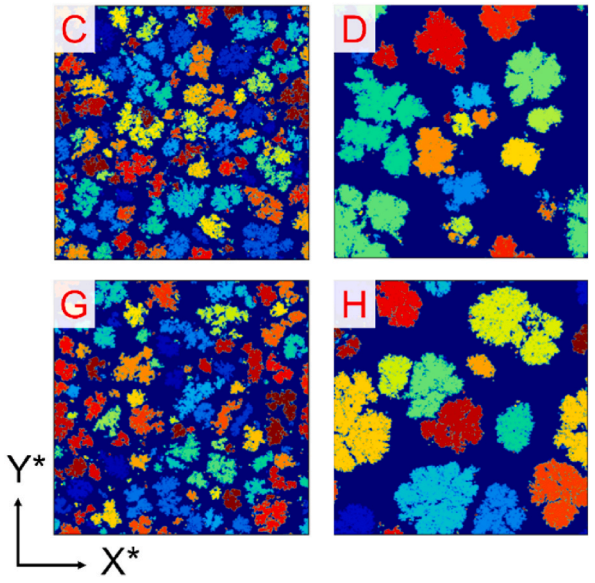

Fig. 11. Individual dendrites identified by DBSCAN when produced under four different conditions, highlighted with arbitrary colors. (For interpretation of the references to color in this figure legend, the reader is referred to the Web version of this article.)

PSDs or the secondary (right) mode radius for the bimodal PSDs at all Kn_D and χ_F combinations. During the structure transition from intermediate to dendrites, for instance, when χ_F decreases from 10^0 to 10^{-1} at $Kn_D = 10^1$, $r^*_{pore,mode}$ in Fig. 9 varies from 2.7 to 8.3, which is a larger increase than $r^*_{pore,geo}$ (changed from 2.4 to 3.8 in Fig. 8). Recalling the PSD profiles of Cases B and C in Fig. 7(a), it is not surprising that the secondary mode radius is more sensitive than the average pore radius to changes in pore structures due to the appearance of dendrites. Additionally, Fig. 9 shows that the red-to-sky blue zone is precisely bounded by the dashed line in contrast to $r^*_{pore,geo}$ in Fig. 8. This suggests that the secondary mode radius is a suitable parameter for characterizing the dendritic structure of nanoparticle deposits by defining the average gap distance between dendrites.

Lastly, we developed a simple model to predict the width of dendrites from the aforementioned structural properties of deposits in terms of $r^*_{pore,geo}$, $r^*_{pore,mode}$, and $\overline{\Theta}_{pore}$. First, we simplify the dendrites to N_{dend} identical cylinders that are uniformly distributed on the floor with a $L \times L$ domain size (see Fig. 10). In this case, the overall porosity of the deposit ($\overline{\Theta}_{pore}$) can be expressed as

$$\overline{\Theta}_{pore} = \frac{\Theta_{pore,dend} V_{dend} + \Theta_{pore,empty} V_{empty}}{V_{sys}} \tag{4}$$

where V_{dend} is the apparent volume occupied by dendrites, V_{empty} is the volume of empty space between dendrites, and V_{sys} is the volume of the overall system (i.e., the middle layer of a deposit). Since the floor is square, the volume fraction of dendrites (V_{dend}/V_{sys}) becomes $N_{dend}\pi w^2/4L^2$, where w is the dendrite width. As shown in the figure, the entire dendritic structure can be regarded as a repetition of a unit cell comprising a single dendrite and its surrounding square pore. Thus, the porosity, i.e., the volume fraction of the empty space (V_{empty}/V_{sys}), can be estimated by the porosity of the unit cell with a side of $L' = L/\sqrt{N_{dend}}$ as: $(V_{sys} - V_{dend})/V_{sys} = (L'^2 - \pi w^2/4)/L'^2$. With the expressions of two volume fractions, Eq. (4) can now be expressed in terms of w and L' as

$$\overline{\Theta}_{pore} = \Theta_{pore,dend}\frac{\pi w^2}{4L'^2} + \Theta_{pore,empty}\frac{4L'^2 - \pi w^2}{4L'^2} \tag{5}$$

Here, the overall porosity ($\overline{\Theta}_{pore}$) is known for each deposition condition. The porosity of empty space between dendrites ($\Theta_{pore,empty}$) was set to be 100%, whereas the porosity inside dendrites ($\Theta_{pore,dend}$) was approximated to be 85% because it was quite similar to the overall porosity of the compact structures (refer to Case A in Table 1). To determine the two unknowns (w, L'), we introduced an additional equation that relates w to L' through the distance between dendrites as follows. Referring to Fig. 10, one may notice that the distance between dendrites has two limiting values, depicted by two (dashed or dotted) circles, which encompass the (dimensional) secondary mode diameter of pores in bimodal PSDs ($d_{pore,mode} = 2r^*_{pore,mode} \bullet r_p$). Hence, we approximated the center-to-center distance between two dendrites, which can vary in a range of L' and $\sqrt{2}L'$ to be the sum of $d_{pore,mode}$ and w as

$$AL' = d_{pore,mode} + w \tag{6}$$

where A is a constant in a range of 1 and $\sqrt{2}$. Combining Eqs. (5) and (6) yields a dimensionless form of equation for calculation of the

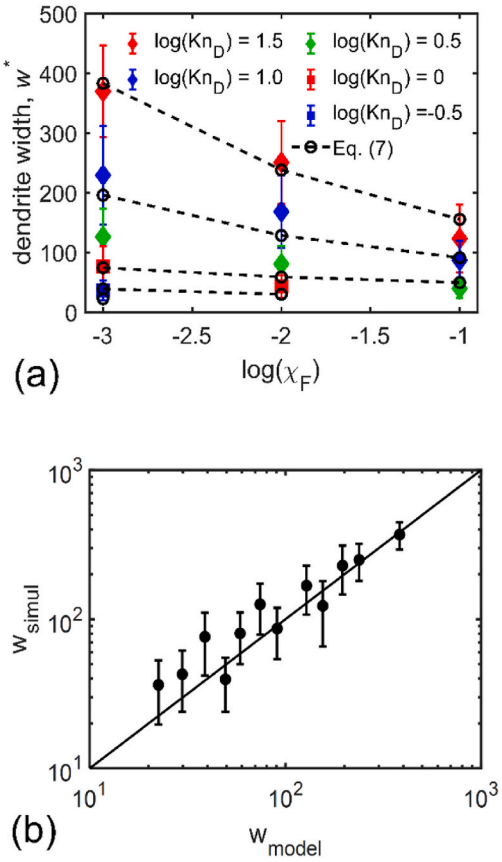

Fig. 12. Validation of the model prediction for the average width of dendrites: (a) Comparison of the predicted average widths of dendrites with those obtained from DBSCAN under different deposition conditions, and (b) A direct comparison of the average width between the model prediction using Eq. (7) and the DBSCAN calculation.

dimensionless width of dendrites w^* ($\equiv w/r_p$) as

$$w^* = \frac{2r^*_{pore,mode}\sqrt{\alpha}}{1-\sqrt{\alpha}} \tag{7}$$

where $\alpha = C(\Theta_{pore,empty} - \overline{\Theta}_{pore})/(\Theta_{pore,empty} - \Theta_{pore,dend})$, and $C = 4/\pi A^2$. In the simplest case depicted by Fig. 10, the parameter C ranges from 0.63 to 1.27, corresponding to the variation in A. Using Eq. (7), it is possible to predict the width of dendrites with a certain value of C in realistic conditions, where irregular dendrites are randomly distributed, as shown in Fig. 7(a) and (c). It is worth noting that a single constant value of $C = 1.15$ was sufficient to achieve the best match with the validation results (will be discussed below).

We used Density-Based Spatial Clustering of Applications with Noise (DBSCAN; Ester et al., 1996) to validate the model predictions. As described in Appendix C, DBSCAN efficiently identifies clusters (dendrites in this study) from dispersed data points based on their spatial proximity and number. To achieve this, we discretized the local porosity distribution data into solid and void by using the overall porosity as a threshold. We then analyzed the data by implementing the built-in dbscan function in MATLAB® with the parameters of $\varepsilon = 3$ and $MinPts = 7$. Fig. 11 visualizes the results of DBSCAN applications to Cases C, D, G, and H in Fig. 7(a) and (c) using random colors. For the resulting individual dendrites, we calculated their cross-section areas and the area-equivalent radii to determine the average width of dendrites for each deposition condition.

Fig. 12(a) displays the results of the dendrite width estimated through DBSCAN for the conditions that yielded discernible dendrites, and compares them with the model predictions. All solid symbols represent the average widths of dendrites obtained by DBSCAN, while the dashed line with open circles indicates the predicted data by Eq. (7). When $\log(Kn_D) = 1.5$, the model predictions are observed to fit best with the validation data obtained by DBSCAN. Even when Kn_D decreases down to $10^{1.0}$, the model predictions are still reasonably accurate. Under these highly-diffusive conditions, the dendrites are sufficiently large and separated enough to be distinguished, so the validation data should be sufficiently reliable. This suggests that the model equation could be used for a priori prediction of the size of dendrites produced once Kn_D and χ_F are predetermined (as the remaining unknown variable, $r^*_{pore,mode}$, in Eq. (7) can be determined from Fig. 9). However, the model starts to underestimate the width of dendrites as Kn_D decreases below $10^{0.5}$, although the predicted average widths of dendrites still lie within the uncertainty range of the validation data. Under these conditions,

smaller dendrites are produced closer to each other, and their branches become entangled, making it difficult to distinguish them with DBSCAN. If this is the case, DBSCAN may overestimate the size of dendrites by merging some pairs of small dendrites into larger ones to some extent. This is in line with the findings that DBSCAN-estimated widths of dendrites are larger than the model predictions when $Kn_D \leq 10^0$. Nevertheless, it should be noted that the model predicts the tendency of change in dendrite width quite well under all experimental conditions. Referring to Fig. 12(b), which directly compares the entire model predictions with the validation data, it can be concluded that the current model can make acceptable predictions of the size of dendrites once they are produced.

5. Conclusion

In this study, we presented, for the first time, the PSDs of nanoparticle deposits in the entire range from dendritic structure to the compact structures, with validation, using Monte Carlo Simulation and Delaunay triangulation method. Under highly advective conditions (e.g., $\chi_F \geq 1$ or $Kn_D \leq 0.1$), the resulting deposits have compact structures with overall porosity $\leq$ 89%, autocorrelation index ≤ 0.4, and unimodal PSDs with a mode radius of ~$2.5\, r_p$. As the condition gradually changes into thermally-dominated condition by increasing Kn_D or decreasing χ_F, the deposit layers were found to undergo gradual changes from compact to dendritic structures through intermediate structures. During the structural changes, we observed a gradual increase in the overall porosity and autocorrelation index, both of which indicate the creation of dendrites. Simultaneously, we confirmed that PSDs became bimodal. As dendrites became larger with an increase in Kn_D or a decrease in χ_F, the primary (left) mode radius of pores in bimodal PSDs hardly varied, suggesting that the pore structure inside individual dendrites was almost invariant. However, the secondary (right) mode radius of pores significantly increased, representing an obvious increase in the gap distance between dendrites. We provided two contour plots of the geometric average radius and secondary mode radius of pores in dendritic structures against χ_F and Kn_D. Finally, we proposed a simple model that is capable of reasonable prediction of average width of dendrites.

Declaration of competing interest

The authors declare that they have no known competing financial interests or personal relationships that could have appeared to influence the work reported in this paper.

Data availability

The authors do not have permission to share data.

Acknowledgements

This research was supported by Basic Science Research Program through the National Research Foundation of Korea (NRF) funded by the Ministry of Education (No. 2020R1A2C2011634) and also by a Korea Institute of Energy Technology Evaluation and Planning (KETEP) grant funded by the Korea government (MOTIE) (20214000000140, Graduate School of Convergence for Clean Energy Integrated Power Generation).

Appendix

A. Delaunay triangulation

Delaunay triangulation is one of the methods of dividing a two-dimensional plane into a set of triangles by connecting given points on the plane with non-crossing straight line segments. An important feature of Delaunay triangulation is that except for the three vertices of any triangle (or tetrahedron for 3D), no other points should be contained within its circumcircle (Sloan, 1993), which is known as 'Delaunay condition'. Fig. A1 shows how to divide the trapezoid comprising 4 vertex points into 2 triangles. Fig. A1(a) illustrates the case where the remaining vertex (indicated by an arrow) located outside a triangle is included in the circumcircle of the triangle, not satisfying the Delaunay condition. In this case, flipping the diagonal from Fig. A1(a) to A1(b) leads to construction of Delaunay triangles by satisfying the Delaunay condition. It can be said that the diagonal flip turns the flat triangles in Fig. A1(a) into near equilateral triangles in such a way as to increase the minimum interior angle of the triangle.

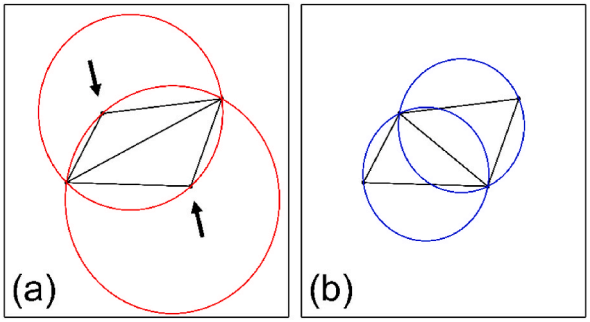

Fig. A1. Example of flipping line segments to meet Delaunay condition: (a) with the condition unsatisfied and (b) with the condition satisfied.

For a set of given points on a flat plane, Delaunay triangulation is progressively implemented in an accordance with the incremental algorithm (Sloan, 1993; Su & Drysdale, 1997) as follows. Starting from listing the coordinates of the whole points, three dummy points are created in a large distance from the set of points to form a super-triangle encompassing all of the points. In Fig. A2, the dotted triangle ABC is the super-triangle that contains 5 original points with IDs of D to H. By adding the given points one by one, the triangulation proceeds sequentially (via flipping if necessary) to satisfy the Delaunay condition. Fig. A2(a) illustrates the result of the Delaunay triangulation for the first 4 points (D, E, F, G).

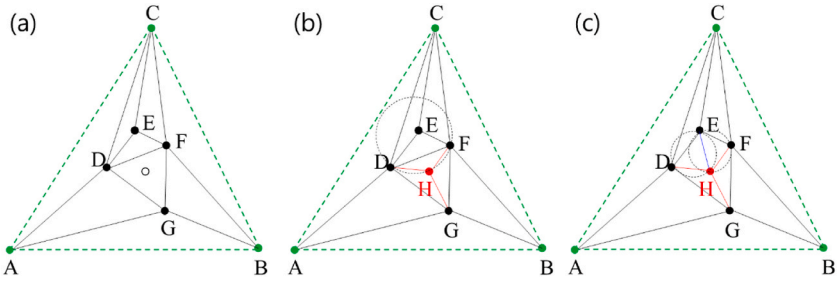

Fig. A2. Illustration of the incremental algorithm for Delaunay triangulation.

Next, the 5th point (H) is added at its coordinate inside the triangle DFG and connected with the three vertices (D, F, G) of the triangle as shown with the red line segments in Fig. A2(b). Because the circumcircle of the new triangle DFH now encompasses the point E in Fig. A2(b), the diagonal DF of the new trapezoid H-DEF is flipped to the line segment EH, which satisfies the Delaunay condition as shown in Fig. A2(c). This test-to-flip process is repeated for the two remaining adjacent trapezoids such as ADHG and BGHF. Then, the foregoing add-to-flip process is continued until all the given points satisfy the Delaunay condition. After the completion of the entire triangulation, the super-triangle and the line segments connected with its dummy points are removed.

We utilized the built-in commands in MATLAB® (Barber et al., 1996) to execute the Delaunay triangulation for the porous layer of nanoparticle deposit as follows. After depositing N_p particles, we recorded their center coordinates in a matrix named ' C'. This matrix served as an input parameter for invoking the intrinsic function 'delaunayTriangulation' as $DT = \mathrm{delaunayTriangulation}(C)$. Here, the returned object DT represents the delaunayTriangulation class in MATLAB, which contains the complete connectivity list of the resulting tetrahedrons. This list specifies the three-dimensional coordinates of the four vertices of each tetrahedron. Following that, we invoked another intrinsic function called 'circumcenter' with the input parameter DT as $[C_{cir}, r_{cir}] = \mathrm{circumcenter}(DT)$. Here, C_{cir} and r_{cir} contain two sets of center coordinates and radii of the circumspheres, respectively.

B. Calculation of a pore volume taken by a tetrahedron generated by Delaunay Triangulation

Following Appendix A, this section explains the procedure for calculating the pore volume occupied by a tetrahedron. Regarding that four spheres of equal size are positioned at the vertices of the tetrahedron, it is necessary to sequentially subtract the overlapping volume between each sphere and the tetrahedron from the total volume of the tetrahedron. This calculation allows us to obtain the accurate volume of the corresponding pore.

The volume of any tetrahedron, denoted as V_{tet}, can be easily calculated by utilizing the cross and dot products of its three edge vectors as $V_{tet} = \frac{1}{3}\left[\frac{1}{2}(\vec{a} \times \vec{b})\right] \bullet \vec{c}$ (refer to the figure on the right in Fig. B1). Now the challenge is to find a simple analytic formula to calculate the overlapping volume between the tetrahedron and the sphere. The overlapping region, represented by a dotted box in the figure, is magnified in a spherical coordinate system centered on the sphere, as shown on the left side of Fig. B1. The three points A, B, and C on the surface of the sphere correspond to the intersection points of the three edge vectors ($\vec{a}$, $\vec{b}$, $\vec{c}$) of the tetrahedron. Consequently, the position vectors ($\vec{u}_1$, $\vec{u}_2$, $\vec{u}_3$) of these points essentially represent the unit vectors (as normalized by the particle radius) that define the polyhedral cone of interest, $OABC$. The cross product ($\vec{v}_{ij}$) of any pair of the position vectors defines the circular cross-section on which they simultaneously exist, as $\vec{v}_{ij} = \vec{u}_i \times \vec{u}_j$ for $(i,j) \in \{1,2,3\}$ and $i \neq j$. Thus, a vertex angle (θ_i) of the formed

spherical triangle *ABC* (highlighted with green color) represents the angle between two circular cross-sections that intersect at the vertex point. The vertex angle can be calculated using the formula $\cos(\theta_i) = \vec{v}_{ij} \bullet \vec{v}_{ik} / (\left|\vec{v}_{ij}\right| \left|\vec{v}_{ik}\right|)$, where the indices (*i, j, k*) take non-repeated integers from the set $\{1, 2, 3\}$. Therefore, knowing the three vertex angles of the spherical triangle, it is straightforward to calculate the area (A_{st}) of the spherical triangle in radians using the formula: $A_{st} = (\theta_1 + \theta_2 + \theta_3 - \pi)R^2$, where $R = 1$. This formula was proven by Leonhard Euler (1707–1783) in 1781 (McCleary, 1994). Note that the sum of the three angles on the convex hull of the spherical triangle is always larger than π, unlike in a planar triangle. Lastly, the volume of the polyhedral cone *OABC* (V_{cone}) is obtained by multiplying A_{st} by $\frac{1}{3}R$ as $V_{cone} = \frac{1}{3}R \bullet A_{st} = \frac{1}{3}(\theta_1 + \theta_2 + \theta_3 - \pi)R^3$. This calculation is then repeated for the three remaining vertices to calculate the total overlapping volume of the tetrahedron.

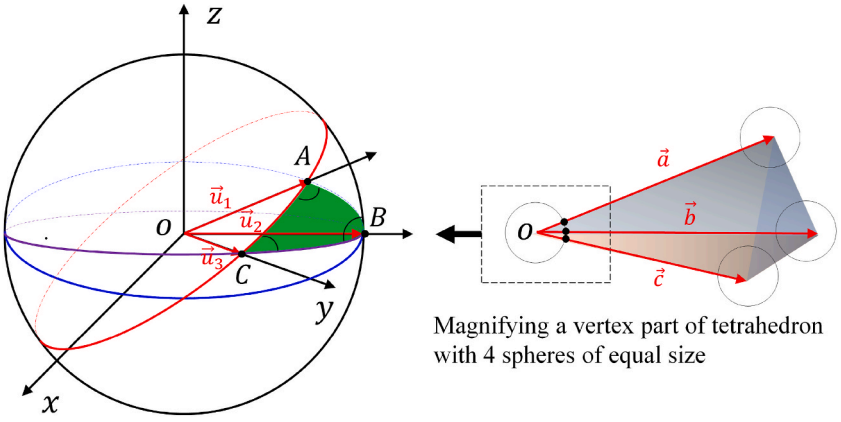

Fig. B1. Spherical coordinate system for identifying the overlapping volume of a tetrahedron and a sphere positioned at a vertex of the tetrahedron.

C. Clustering algorithm

DBSCAN (Density-Based Spatial Clustering of Applications with Noise) is one of the most popular clustering algorithms. It identifies arbitrary-shaped clusters using two density parameters: ε and *MinPts*. Given an input data set, the algorithm performs the ε-neighborhood query to identify three kinds of data points: core points, border points, and noise points (Ester et al., 1996) according to the following steps:

1) Select the first unlabeled point as the current point.
2) Find the set of points within the radius of ε of the current point. These points are the neighbors. If the number of neighbors is equal to or larger than *MinPts*, then label the current point as a core point of the first cluster.
3) Iterate Step 2 for each neighbor (as a new current point) until all the neighbors are tested. Some of the original neighbors, if they have fewer than *MinPts* new neighbors, are labelled as border points. So the first cluster comprises core points and border points.
4) Select a new unlabeled point and repeat Steps 2–3 to identify other clusters until no unselected points are left. Any selected but yet unlabeled points are treated as outliers or noise points.

If two clusters are close to each other, that is, the distance between two border points (one from each cluster) is less than ε, DBSCAN merges the two clusters into one. As such, the identified clusters can be visualized by differentiating them using arbitrary colors, and the number of constituent points and the apparent area or size of each cluster can be calculated.

Appendix A. Supplementary data

Supplementary data to this article can be found online at https://doi.org/10.1016/j.jaerosci.2023.106227.

References

Al-Raoush, R., Thompson, K., & Willson, C. S. (2003). Comparison of network generation techniques for unconsolidated porous media. *Soil Science Society of America Journal, 67*(6), 1687–1700.
Barber, C. B., Dobkin, D. P., & Huhdanpaa, H. (1996). The quickhull algorithm for convex hulls. *ACM Transactions on Mathematical Software, 22*(4), 469–483.
Baturina, O. A., & Wnek, G. E. (2005). Characterization of proton exchange membrane fuel cells with catalyst layers obtained by electrospraying. *Electrochemical and Solid-State Letters, 8*(6), A267.
Bhattacharya, S., & Gubbins, K. E. (2006). Fast method for computing pore size distributions of model materials. *Langmuir, 22*(18), 7726–7731.
Cai, Y., Tay, K., Zheng, Z., Yang, W., Wang, H., Zeng, G., Li, Z., Siah, B., & Subbaiah, P. (2018). Modeling of ash formation and deposition processes in coal and biomass fired boilers: A comprehensive review. *Applied Energy, 230*, 1447–1544.

Castillo, J. L., Martin, S., Rodriguez-Perez, D., Perea, A., & Garcia-Ybarra, P. L. (2014). Morphology and nanostructure of granular materials built from nanoparticles. *KONA Powder and Particle Journal, 31*, 214–233.
Cherevko, S., & Chung, C. H. (2011). Direct electrodeposition of nanoporous gold with controlled multimodal pore size distribution. *Electrochemistry Communications, 13*(1), 16–19.
Dreyer, J. A., Riefler, N., Pesch, G. R., Karamehmedović, M., Fritsching, U., Teoh, W. Y., & Mädler, L. (2014). Simulation of gas diffusion in highly porous nanostructures by direct simulation Monte Carlo. *Chemical Engineering Science, 105*, 69–76.
Ermak, D. L., & Buckholtz, H. (1980). Numerical integration of the Langevin equation: Monte Carlo simulation. *Journal of Computational Physics, 35*, 169–182.
Ester, M., Kriegel, H. P., Sander, J., & Xu, X. (1996). A density-based algorithm for discovering clusters in large spatial databases with noise. *Proceedings of the Second International Conference on Knowledge Discovery and Data Mining*, 226–231 *(KDD'96)*.
German, R. M. (2014). *Sintering: From empirical observations to scientific principles*. Butterworth-Heinemann.
Gopalakrishnan, R., & Hogan, C. J., Jr. (2011). Determination of the transition regime collision kernel from mean first passage times. *Aerosol Science and Technology, 45*, 1499–1509.
Hinds, W. C. (1999). *Aerosol technology: Properties, behavior, and measurement of airborne particles*. John Wiley & Sons.
Hunt, B., Thajudeen, T., & Hogan, C. J., Jr. (2014). The single-fiber collision rate and filtration efficiency for nanoparticles I: The first-passage time calculation approach. *Aerosol Science and Technology, 48*(8), 875–885.
Kim, J., Shin, J., & Lee, D. (2022). Microstructural transition of nanoparticle deposits from multiple dendrites to compact layer. *Journal of Aerosol Science, 159*(1–16), Article 105876.
Kruyer, S. (1958). The penetration of mercury and capillary condensation in packed spheres. *Transactions of the Faraday Society, 54*, 1758–1767.
Kubo, M., Ishihara, Y., Mantani, Y., & Shimada, M. (2013). Evaluation of the factors that influence the fabrication of porous thin films by deposition of aerosol nanoparticles. *Chemical Engineering Journal, 232*, 221–227.
Kulkarni, P., & Biswas, P. (2004). A Brownian dynamics simulation to predict morphology of nanoparticle deposits in the presence of interparticle interactions. *Aerosol Science and Technology, 38*(6), 541–554.
Lee, J., & Hogan, C. J., Jr. (2021). Computational predictions of porosities, pore size distributions, and conductivities of aerosol deposited particulate films. *Powder Technology, 378*, 400–409.
Lindquist, G. J., Pui, D. Y., & Hogan, C. J., Jr. (2014). Porous particulate film deposition in the transition regime. *Journal of Aerosol Science, 74*, 42–51.
Li, Y., Vu, N., & Kim, A. S. (2009). 3-D Monte Carlo simulation of particle deposition on a permeable surface. *Desalination, 249*(1), 416–422.
Mädler, L., & Friedlander, S. K. (2007). Transport of nanoparticles in gases: Overview and recent advances. *Aerosol and Air Quality Research, 7*(3), 304–342.
Mädler, L., Lall, A. A., & Friedlander, S. K. (2006). One-step aerosol synthesis of nanoparticle agglomerate films: Simulation of film porosity and thickness. *Nanotechnology, 17*(19), 4783.
McCleary, J. (1994). *Geometry from a differentiable viewpoint* (Cambridge).
Morales-Flórez, V., Piñero, M., De La Rosa-Fox, N., Esquivias, L., Anta, J. A., & Primera, J. (2008). The cluster model: A hierarchically-ordered assemblage of random-packing spheres for modelling microstructure of porous materials. *Journal of Non-crystalline Solids, 354*(2–9), 193–198.
Morán, J., Yon, J., & Poux, A. (2020). Monte Carlo aggregation code (mcac) part 1: Fundamentals. *Journal of Colloid and Interface Science, 569*, 184–194.
Nasiri, N., Elmøe, T. D., Liu, Y., Qin, Q. H., & Tricoli, A. (2015). Self-assembly dynamics and accumulation mechanisms of ultra-fine nanoparticles. *Nanoscale, 7*(21), 9859–9867.
Nuvoli, J., Bourrous, S., Ouf, F. X., & Thomas, D. (2021). Measurement of the porosity of a pseudo-spherical nanostructured particle deposit formed by filtration. *Journal of Aerosol Science, 151*, Article 105681.
Ou, Q. (2013). *Aerosol filtration–agglomerate particle filtration and particle deposition uniformity*. St. Louis: *Ph.D. Thesis*, Washington University.
Primera, J., Hasmy, A., & Woignier, T. (2003). Numerical study of pore sizes distribution in gels. *Journal of Sol-Gel Science and Technology, 26*(1), 671–675.
Rodríguez-Pérez, D., Castillo, J. L., & Antoranz, J. C. (2005). Relationship between particle deposit characteristics and the mechanism of particle arrival. *Physical Review, 72*(2), Article 021403.
Rodriguez-Perez, D., Castillo, J. L., & Antoranz, J. C. (2007). Density scaling laws for the structure of granular deposits. *Physical Review, 76*(1), Article 011407.
Schmidt, E. (1996). Simulation of three-dimensional dust structures via particle trajectory calculations for cake-forming filtration. *Powder Technology, 86*(1), 113–117.
Shin, H. C., Dong, J., & Liu, M. (2003). Nanoporous structures prepared by an electrochemical deposition process. *Advanced Materials, 15*(19), 1610–1614.
Sloan, S. W. (1993). A fast algorithm for generating constrained Delaunay triangulations. *Computers & Structures, 47*(3), 441–450.
Storchi, L., De Angelis, F., & Nunzi, F. (2015). Modeling mesoporous nanoparticulated TiO2 films through nanopolyhedra random packing. *Journal of Physical Chemistry C, 119*(19), 10716–10726.
Su, P., & Drysdale, R. L. S. (1997). A comparison of sequential Delaunay triangulation algorithms. *Computational Geometry, 7*(5–6), 361–385.
Tassopoulos, M., O'Brien, J. A., & Rosner, D. E. (1989). Simulation of microstructure/mechanism relationships in particle deposition. *AIChE Journal, 35*(6), 967–980.
Tricoli, A., Graf, M., Mayer, F., Kuühne, S., Hierlemann, A., & Pratsinis, S. E. (2008). Micropatterning layers by flame aerosol deposition-annealing. *Advanced Materials, 20*(16), 3005–3010.
Wang, Y., Wang, X., Wang, X., Liu, T., Zhu, T., Liu, S., & Qin, Y. (2021). Droplet dynamic characteristics on PEM fuel cell cathode gas diffusion layer with gradient pore size distribution. *Renewable Energy, 178*, 864–874.
Xiong, Q., Baychev, T. G., & Jivkov, A. P. (2016). Review of pore network modelling of porous media: Experimental characterisations, network constructions and applications to reactive transport. *Journal of Contaminant Hydrology, 192*, 101–117.
Yang, Z., Peng, X. F., Lee, D. J., & Chen, M. Y. (2009). An image-based method for obtaining pore-size distribution of porous media. *Environmental Science & Technology, 43*(9), 3248–3253.
Zeng, S. Q., Hunt, A. J., Cao, W., & Greif, R. (1994). Pore size distribution and apparent gas thermal conductivity of silica aerogel. *Journal of Heat Transfer, 116*(3), 756, 659.
Zhang, T., & Lin, G. (2007). A decomposition of Moran's I for clustering detection. *Computational Statistics & Data Analysis, 51*(12), 6123–6137.